Letter

Pressure-induced ferroelectric-to-superconductor transition in $SnPS_3$

Binbin Yue,[1,*] Wei Zhong,[1] Ting Wen,[1] Yonggang Wang,[1] Hui Yu,[2,3] Xiaohui Yu,[2,3,4] Changfeng Chen,[5] Jian-Tao Wang,[2,3,4,†] and Fang Hong[2,3,4,‡]

[1]*Center for High Pressure Science & Technology Advanced Research, Haidian, Beijing 100094, China*
[2]*Beijing National Laboratory for Condensed Matter Physics and Institute of Physics, Chinese Academy of Sciences, Beijing 100190, China*
[3]*School of Physical Sciences, University of Chinese Academy of Sciences, Beijing 100049, China*
[4]*Songshan Lake Materials Laboratory, Dongguan, Guangdong 523808, China*
[5]*Department of Physics and Astronomy, University of Nevada, Las Vegas, Nevada 89154, USA*

(Received 24 December 2022; revised 26 March 2023; accepted 29 March 2023; published 7 April 2023)

Ferroelectricity and superconductivity are prominent yet distinct quantum phenomena; materials exhibiting both of these phenomena are rare and of great fundamental and practical interest. Here, combining *ab initio* calculations and *in situ* measurements, we show that ferroelectric $SnPS_3$ turns into a superconductor under pressure at 31.7 GPa, accompanied by a structural phase transition. Electronic band structure calculations reveal a partial flat band near the Fermi energy in compressed $SnPS_3$, suggesting correlation effects as a possible origin of the observed superconducting state. The discovery of a pressure-induced ferroelectric-to-superconductor transition in $SnPS_3$ raises the prospect of establishing this intriguing quantum phenomenon among a large class of metal phosphorous trichalcogenides, thereby broadening the material basis to elucidate the underlying physics.

DOI: 10.1103/PhysRevB.107.L140501

Metal phosphorous trichalcogenides MPX_3 are a large family of layered materials comprising metal cations in a stabilized $[P_2X_6]^{4-}$ framework that bond to each other via weak van der Waals interactions [1–4]. The metal (M) elements include transition metals (e.g., V, Cr, Mn, Fe, Co, Ni, Cu, Zn, Cd, Hg, Pd, and Ag), post-transition metals (e.g., In, Ga, Sn, and Pb) and alkali metals (e.g., Mg and Ca); the chalcogen (X) elements currently include only S and Se. Most of these compounds adopt a monoclinic or rhombohedral lattice structure derived from the $CdCl_2$ and CdI_2 structural type with different stacking of individual layers. These compounds are mostly either semiconductors or insulators with the electronic band gap between 1.3 and 3.5 eV [5–7], allowing optoelectronic applications in a broad wavelength range. In addition, magnetic properties and intercalation-substitution behaviors in various MPX_3 compounds also have attracted attention for their potential applications in spintronic devices [4,8], batteries [9], and catalysis [10].

Previous works demonstrated that the electronic properties of MPX_3 can be tuned via chemical doping [11,12], temperature [13], or pressure/stress [14–21]. The introduction of copper in $SnPS_3$ has a major impact on the shape smearing of ferroelectric domains and on the behavior of dielectric permittivity [12]. Trisulfide compounds with M = Mn, Fe, Co, and Ni are paramagnetic at high temperatures and undergo a transition to an antiferromagnetic state upon cooling [13]. High-pressure studies on several MPX_3 materials, including $FePS_3$, $FePSe_3$, $MnPS_3$, $MnPSe_3$, $NiPS_3$, and $V_{0.9}PS_3$, revealed interesting phenomena including a Mott metal-to-insulator transition, spin crossover, and volume collapse [14–21]. More interestingly, superconductivity emerges at around 3 K in the nonmagnetic high-pressure phase of $FePSe_3$ above ~9 GPa [15]. Such a pressure-induced superconducting (SC) transition is known to exist in metal chalcogenides, such as MoS_2 [22], $SnSe_2$ [23], and HfS_3 [24], but $FePSe_3$ is the only known MPX_3 compound to show a SC transition [15]. Identifying more high-pressure superconducting MPX_3 compounds is the key to exploring this intriguing phenomenon and elucidating the underlying mechanism.

In this Letter, we report the discovery of a pressure-induced ferroelectric-to-superconductor transition in $SnPS_3$, which has an electronic band gap of ~2.3 eV and crystallizes in a monoclinic Pc (C_s^2, No. 7) structure at ambient condition [25–27]. The Sn^{2+} cations and $[P_2S_6]^{4-}$ anion clusters are joined by ionic Sn-S bonds while the intracluster P-S and P-P bonds are of a covalent nature [26,28]. This compound undergoes a second-order transition from the ferroelectric phase to a paraelectric phase in $P2_1/c$ (C_s^5, No. 14) symmetry around a pressure of 0.2–0.5 GPa [29–31]. Combining *ab initio* calculations and *in situ* high-pressure x-ray diffraction measurements, we identified a metallic monoclinic phase in $P2_1$ (C_2^2, No. 4) symmetry above 31.7 GPa. Low-temperature transport measurements show that $SnPS_3$ remains a semiconductor up to 31.7 GPa, above which the compound enters a SC state with a critical temperature of 2.2 K, which increases slightly to ~2.8 K at 48.9 GPa. The SC transition coincides with a structural phase transition from $P2_1/c$ to $P2_1$ symmetry. The upper critical field is estimated to be 3.03 T by fitting the T_c-H curve via the Ginzburg-Landau (GL) equation. Electronic band structure calculations reveal a partial flat band near the Fermi energy in the $P2_1$ phase, suggesting that the SC

*yuebb@hpstar.ac.cn
†wjt@aphy.iphy.ac.cn
‡hongfang@iphy.ac.cn

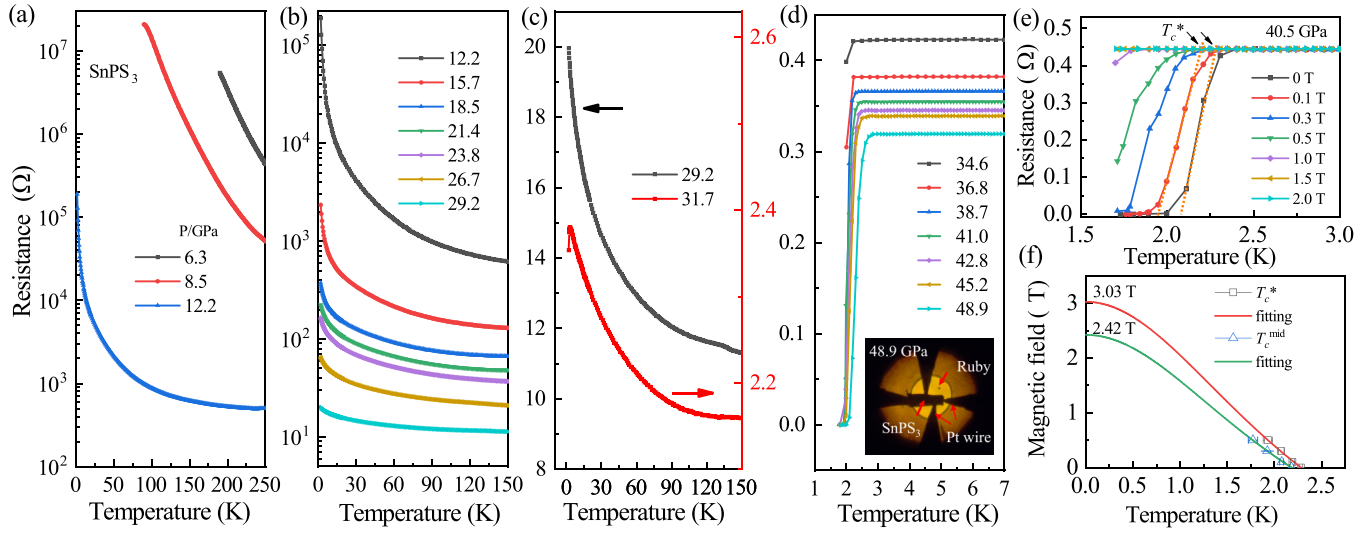

FIG. 1. The electrical transport properties of $SnPS_3$ under pressure. (a)–(d) Temperature-dependent resistance (R-T) of $SnPS_3$ single crystal under various pressures up to 48.9 GPa. The insulator-to-superconductor transition at low temperature is shown around 31.7 GPa. The inset in (d) shows an image of the standard four-probe electrical resistance measurement set up in the DAC chamber. (e) The R-T curves at various magnetic fields near the superconducting transition region at 40.5 GPa. (f) The upper critical magnetic field–temperature relation extracted from (e), and the corresponding GL equation fitting result (red and green lines). Note: The determination of T_c^* is shown in (e). T_c^{mid} is the temperature when R is equal to $R_{3\,\mathrm{K}}/2$, which is ∼0.22 Ω.

state may be driven by correlation effects. The present results raise the prospect of finding pressure-induced superconductivity in the large MPX_3 family, thus expanding the material basis for a more in-depth exploration of pertinent quantum phenomena.

We performed electrical resistance measurements using the standard four-probe methods in the temperature range from 1.7 to 300 K and under pressure up to 48.9 GPa achieved using a BeCu diamond anvil cell (DAC). Structural evolution was examined by *in situ* x-ray powder diffraction (XRD) and Raman spectroscopy, while ultraviolet-to-visible-to-near-infrared (UV-vis-NIR) absorption spectroscopy was employed to probe the optical properties. Density functional theory (DFT) calculations were performed using the Vienna *ab initio* simulation package (VASP) [32] with the all-electron projector augmented-wave method [33]. The Perdew-Burke-Ernzerhof revised for solids (PBEsol) [34] exchange-correlation functional was adopted for the evaluation of structural stability. Electronic band structures and density of states were calculated using the modified Becke-Johnson (mBJ) functional [35]. Detailed information about the experimental and computational methods is provided in Supplemental Material [36].

The $SnPS_3$ single crystal shows a dark amber color in the ambient environment and adopts a monoclinic structure in Pc (C_s^2, No. 7) symmetry. The crystal quality was checked by XRD and transmission scanning microscopy, as presented in Fig. S1 in Supplemental Material [36]. The measured electric transport properties of the $SnPS_3$ single crystal under pressure up to 48.9 GPa are presented in Fig. 1. The initial resistance of the sample is too large to be detected by our multimeter (the maximum limit is 200 MΩ), reflecting its insulating nature. When pressure is increased to 6.3 GPa, room-temperature resistance becomes measurable with a value of ∼10.6 kΩ. The resistance increases rapidly upon cooling and becomes out of range when the temperature is lower than ∼190 K, as shown in Fig. 1(a). Upon further compression, the resistance declines quickly, and it is reduced by more than four orders of magnitude at 100 K at 12.2 GPa, compared with that at 8.5 GPa. Meanwhile, the $R-T$ data can be collected at the whole temperature range at 12.2 GPa. Above 15.7 GPa, the decreasing trend of the resistance slows down but the $R-T$ curves always show a typical semiconducting behavior until 31.7 GPa, as shown in Figs. 1(b) and 1(c). Starting from 31.7 GPa, a sudden drop of resistance is observed around 2.2 K [see Figs. 1(c) and 1(d)], indicating a possible SC transition, which is enhanced at higher pressures. The zero-resistance state is observed above 38.7 GPa, and T_c slightly increases to ∼2.8 K at 48.9 GPa.

To confirm pressure-induced superconductivity in $SnPS_3$, we measured temperature-dependent resistance at 40.5 GPa in external magnetic fields up to 2 T. Results [Fig. 1(e)] show that T_c is progressively suppressed by increasing magnetic field, which is typical for a SC transition, and superconductivity is absent above 1.5 T down to the lowest measured temperature of 1.7 K. The upper critical field $\mu_0 H_{c2}$ vs T_c (T_c^* and T_c^{mid}) is shown in Fig. 1(f). Fitting the $\mu_0 H_{c2}$-T_c^* relation with the GL equation [37] gives $\mu_0 H_{c2}(0)$ of 3.03 T, which is lower than the Bardeen-Copper-Schrieffer (BCS) weak-coupling Pauli paramagnetic limit of $\mu_0 H_p = 1.84 T_c = 4.2$ T for $T_c = 2.28$ K, suggesting the absence of Pauli pair breaking [38]. Also, a lower $\mu_0 H_{c2}(0) = 2.42$ T is obtained if using the T_c^{mid} as the fitting data in Fig. 1(f).

To elucidate the observed transport behaviors, especially the SC transition, we examined the structural evolution of $SnPS_3$ under pressure by XRD, as shown in Fig. 2(a). The ambient ferroelectric Pc phase transforms to the paraelectric $P2_1/c$ phase at 0.2–0.5 GPa [29,30]. The XRD patterns of the Pc and $P2_1/c$ phases are similar, thus unable to pinpoint the phase transition pressure; but the optical band gap extracted from the absorption spectroscopy shows a sudden drop near

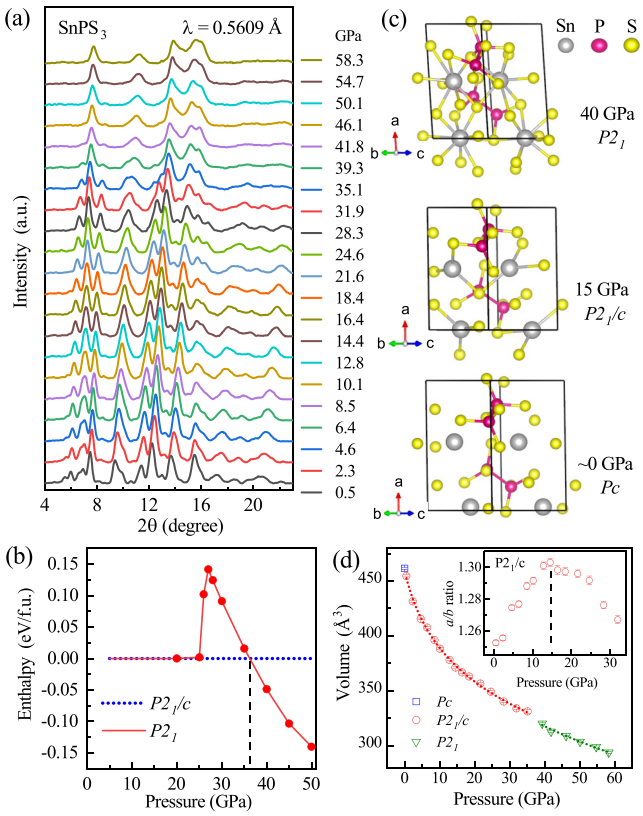

FIG. 2. Structural evolution of $SnPS_3$ under pressure. (a) The integrated XRD pattern up to 58.3 GPa. The x-ray wavelength $\lambda = 0.5609$ Å. (b) Relative enthalpy between the $P2_1/c$ and $P2_1$ phases. The red line shows a reversible conversion upon decompression from the high-pressure $P2_1$ phase. (c) The lattice structure of $SnPS_3$ in Pc (No. 7), $P2_1/c$ (No. 14), and $P2_1$ (No. 4) symmetry at 0, 15, and 40 GPa, respectively. (d) The pressure-volume relation of $SnPS_3$ under pressure. The inset shows the a/b ratio for the $P2_1/c$ phase.

0.42 GPa, signaling the Pc-$P2_1/c$ transition, as shown in Fig. S2 in Supplemental Material [36]. The $P2_1/c$ phase is stable up to 31.9–35.1 GPa, above which the intensity of some diffraction peaks (such as 6°–6.5°, 7°–8.5°) notably weakens, suggesting a structural phase transition. Raman spectroscopy, which is more sensitive to the local atomic environment, was also collected. The results (Fig. S3 in Supplemental Material [36]) show that this structural phase transition occurs near ~32.5 GPa, above which Raman signals become nearly invisible. The suppression of Raman modes by pressure indicates a metallization behavior [39,40], which is consistent with the results of the electrical transport measurements. These results show that the metallization and superconductivity in compressed $SnPS_3$ are rooted in the structural phase transition. Moreover, in the Raman experiment, all modes go back to those of the original phase upon pressure release (see Fig. S3 in Supplemental Material [36]), indicating that the pressure-driven structural transition is reversible.

To corroborate and elucidate the pressure-driven structural phase transition in $SnPS_3$, we performed *ab initio* calculations, and the obtained results identify a monoclinic phase in $P2_1$ (C_2^2, No. 4) symmetry that becomes more stable than the $P2_1/c$ phase above ~36 GPa [see Fig. 2(b)]. Similar to the original Pc phase [Fig. 2(c)], the $P2_1$ phase has a 20-atom monoclinic unit cell comprising 12 S, 4 P, and 4 Sn atoms; but in the Pc unit cell, the P and S atoms form two S_3P-PS_3 molecular clusters joined by mostly ionic Sn-S bonds [26,28], while in the $P2_1$ structure, the bond length and angle in S_3P-PS_3 clusters are notably changed during the structural phase transition around 30–35 GPa (see Fig. S4 in Supplemental Material [36]), which weaken the P-P and S-P covalent bonds in the S_3P-PS_3 clusters and enhance the metallic bonding between the S and Sn atoms. The lattice parameters of the $SnPS_3$ crystal at 40 GPa are estimated to be $a = 8.2994$ Å, $b = 6.1040$ Å, $c = 5.5827$ Å, and $\beta = 94.96°$ (more information about the structure is given in Table S1 in Supplemental Material [36]). We also calculated the phonon dispersion under 40 GPa, and the obtained results (see Fig. S5 in Supplemental Material [36]) show no imaginary frequency in the entire Brillouin zone, confirming the dynamical stability of the $P2_1$ phase under high pressure. Moreover, this phase goes back to the original phase automatically when pressure is released [see Fig. 2(b)], which is consistent with the findings of our Raman measurements. The corroboration of these pertinent theoretical and experimental results makes a compelling case that the $P2_1$ structure is the likely structural form for the high-pressure phase of $SnPS_3$.

The equation of state (pressure-volume relation) of $SnPS_3$ is presented in Fig. 2(d); the inset displays the a/b ratio change under pressure for the $P2_1/c$ phase. The a/b ratio shows a kink near ~14 GPa, indicating a lattice distortion of the $P2_1/c$ phase under pressure, and this is also matched with the transport behavior observed around 12.2–15.7 GPa in Fig. 1, at which the resistance at 100 K declined by more than four orders of magnitude, compared with the result obtained at 8.5 GPa. Meanwhile, the optical band gaps extracted from the absorption spectroscopy show a kink near ~14 GPa as well, as shown in Fig. S2 in Supplemental Material [36]. This kind of lattice compression-induced anomalous behavior is often observed in layered materials, such as Bi_2Se_3 [41]. Detailed information about the pressure-dependent lattice parameters is shown in Fig. S6 in Supplemental Material [36].

We further calculated the electronic band structures and partial density of states (DOS) of $SnPS_3$. Results in Fig. 3(a) show that the electronic band gap is ~2.28 eV at 0.0 GPa for the Pc phase, in good agreement with our experimental data of 2.21 eV [see Fig. S2(d) in Supplemental Material [36]], and the band gap is reduced to ~0.32 eV at 30 GPa for the $P2_1/c$ phase, as shown in Fig. 3(b). These results show that pressure is highly effective in suppressing the band gap of $SnPS_3$. Moreover, in the high-pressure $P2_1$ phase, the band gap is closed at 35 GPa with valence and conduction band crossing [see Fig. 3(c)], and further compression up to 50 GPa does not affect the band structure too much. Interestingly, it is noted that there is a partial flat band near the Fermi energy between the high symmetric points A, B, and D, which is mainly contributed by the S and Sn atoms and results in a notable DOS at the Fermi level, as shown in Fig. 3(c). It is known that flat electronic bands tend to produce novel emergent physical behaviors stemming from the strong electron correlation effects, and superconductivity is a prominent case [42,43], which deserves more in-depth investigation to

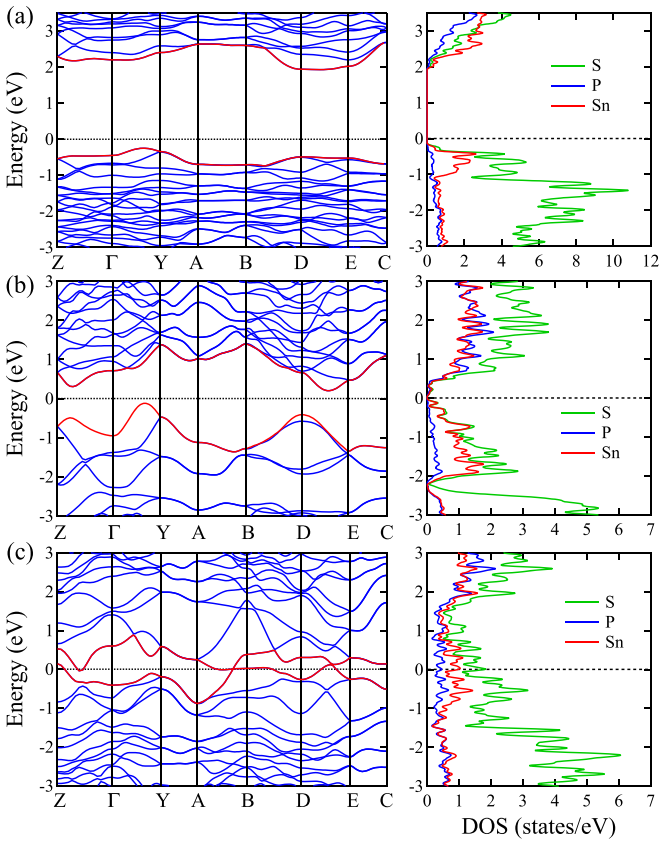

FIG. 3. Calculated electronic band structures and partial DOS for $SnPS_3$ under pressure. (a) At 0 GPa in Pc symmetry, (b) at 30 GPa in $P2_1/c$ symmetry, and (c) at 35 GPa in $P2_1$ symmetry. The highest valence band and lowest conduction band are marked in red.

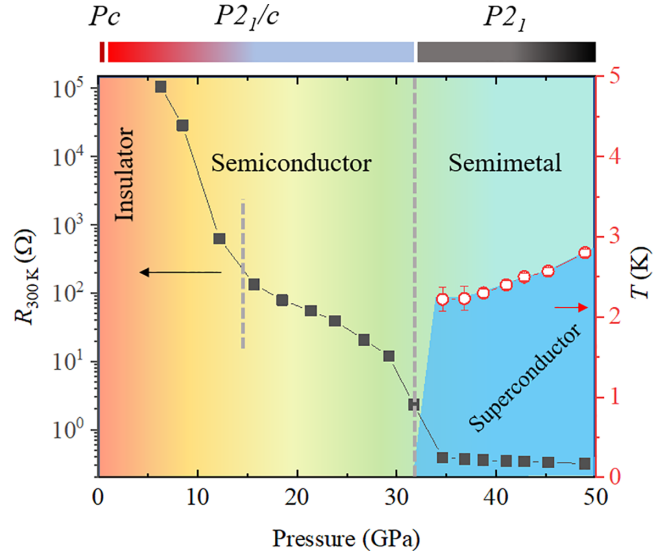

FIG. 4. The pressure-temperature phase diagram of $SnPS_3$ constructed based on the experimental results. Black squares represent the measured resistance of $SnPS_3$ at 300 K. Red circles mark the measured T_c. Dashed lines at ~14 and 31.7 GPa are guides to the eye, where the electronic and/or structural anomalies occur, indicating lattice distortion and a phase transition from the $P2_1/c$ to $P2_1$ phase, respectively.

explore the underlying microscopic mechanisms with broader implications.

Based on our experimental results, we constructed a pressure-temperature phase diagram for $SnPS_3$ shown in Fig. 4. At low pressures, $SnPS_3$ behaves as an insulator with a large electrical resistance, which is out of the detection limit ($\sim 10^8$ Ω) in our experimental setup. Under increasing pressure, $SnPS_3$ turns into a semiconductor and then a semimetal. The pressure-dependent room-temperature resistivity ($R_{300\,\mathrm{K}}$) shows two notable drops near ~14 and 31.7 GPa, related to the lattice distortion of $P2_1/c$ phase [see Fig. 2(d)] and a phase transition from the $P2_1/c$ to $P2_1$ phase [see Fig. 2(b)], respectively. Meanwhile, low-temperature measurements reveal superconductivity from 31.7 to 48.9 GPa with T_c of ~2.2 to ~2.8 K in the $P2_1$ phase.

In summary, combining *ab initio* calculations and *in situ* measurements, we have established compelling evidence for a pressure-induced transition to superconductivity in ferroelectric $SnPS_3$. This phenomenon is rooted in a structural transition from the $P2_1/c$ to $P2_1$ phase, accompanied by the formation of Sn-S metallic bonds. The superconducting behavior remains robust with T_c rising from ~2.2 K at 31.7 GPa to ~2.8 K at 48.9 GPa. $SnPS_3$ is the first compound among the ternary sulfide family exhibiting superconductivity confirmed by experiment. These results may stimulate further experimental and theoretical efforts to explore the large MPX_3 family of compounds, with the prospects of expanding the scope of the material basis for studying pressure-induced superconducting transitions in ferroelectrics. Furthermore, the presence of a partial flat band in $SnPS_3$ provides another platform to probe emergent quantum behaviors stemming from strong electron correlation effects.

This work was supported by the National Key R&D Program of China (Grants No. 2021YFA1400300 and No. 2020YFA0711502), the Major Program of National Natural Science Foundation of China (Grants No. 22090041 and No. 92263202), the National Natural Science Foundation of China (Grants No. 12004014, No. U1930401, and No. 11974387), and the Strategic Priority Research Program of the Chinese Academy of Sciences (Grant No. XDB33000000).

[1] R. Gusmão, Z. Sofer, and M. Pumera, Angew. Chem. Int. Ed. **58**, 9326 (2019).
[2] V. Grasso and L. Silipigni, Riv. Nuovo Cimento **25**, 1 (2002).
[3] F. Wang, T. A. Shifa, P. Yu, P. He, Y. Liu, F. Wang, Z. Wang, X. Zhan, X. Lou, F. Xia, and J. He, Adv. Funct. Mater. **28**, 1802151 (2018).
[4] G. R. Bhimanapati, Z. Lin, V. Meunier, Y. Jung, J. Cha, S. Das, D. Xiao, Y. Son, M. S. Strano, V. R. Cooper, L. Liang, S. G. Louie, E. Ringe, W. Zhou, S. S. Kim, R. R. Naik, B. G. Sumpter, H. Terrones, F. Xia, Y. Wang *et al.*, ACS Nano **9**, 11509 (2015).
[5] K.-Z. Du, X.-Z. Wang, Y. Liu, P. Hu, M. I. B. Utama, C. K. Gan, Q. Xiong, and C. Kloc, ACS Nano **10**, 1738 (2016).

[6] J. Liu, X.-B. Li, D. Wang, W.-M. Lau, P. Peng, and L.-M. Liu, J. Chem. Phys. **140**, 054707 (2014).

[7] M. A. Susner, M. Chyasnavichyus, M. A. McGuire, P. Ganesh, and P. Maksymovych, Adv. Mater. **29**, 1602852 (2017).

[8] X. Jiang, Q. Liu, J. Xing, N. Liu, Y. Guo, Z. Liu, and J. Zhao, Appl. Phys. Rev. **8**, 031305 (2021).

[9] Q. Liang, Y. Zheng, C. Du, Y. Luo, J. Zhao, H. Ren, J. Xu, and Q. Yan, ACS Nano **12**, 12902 (2018).

[10] Z. Cheng, M. G. Sendeku, and Q. Liu, Nanotechnology **31**, 135405 (2020).

[11] X. Li, X. Wu, and J. Yang, J. Am. Chem. Soc. **136**, 11065 (2014).

[12] V. Shvalya, J. Zavašnik, V. Nasretdinova, H. Uršič, J. Kovač, A. Grabar, A. Kohutych, A. Molnar, D. R. Evans, D. D. Mihailovič, and U. Cvelbar, J. Mater. Chem. C **8**, 9975 (2020).

[13] C. C. Mayorga-Martinez, Z. Sofer, D. Sedmidubský, Š. Huber, A. Y. S. Eng, and M. Pumera, ACS Appl. Mater. Interfaces **9**, 12563 (2017).

[14] H.-S. Kim, K. Haule, and D. Vanderbilt, Phys. Rev. Lett. **123**, 236401 (2019).

[15] Y. Wang, J. Ying, Z. Zhou, J. Sun, T. Wen, Y. Zhou, N. Li, Q. Zhang, F. Han, Y. Xiao, P. Chow, W. Yang, V. V. Struzhkin, Y. Zhao, and H.-K. Mao, Nat. Commun. **9**, 1914 (2018).

[16] M. J. Coak, D. M. Jarvis, H. Hamidov, C. R. S. Haines, P. L. Alireza, C. Liu, S. Son, I. Hwang, G. I. Lampronti, D. Daisenberger, P. Nahai-Williamson, A. R. Wildes, S. S. Saxena, and J.-G. Park, J. Phys.: Condens. Matter **32**, 124003 (2020).

[17] C. R. S. Haines, M. J. Coak, A. R. Wildes, G. I. Lampronti, C. Liu, P. Nahai-Williamson, H. Hamidov, D. Daisenberger, and S. S. Saxena, Phys. Rev. Lett. **121**, 266801 (2018).

[18] Y. Wang, Z. Zhou, T. Wen, Y. Zhou, N. Li, F. Han, Y. Xiao, P. Chow, J. Sun, M. Pravica, A. L. Cornelius, W. Yang, and Y. Zhao, J. Am. Chem. Soc. **138**, 15751 (2016).

[19] M. J. Coak, S. Son, D. Daisenberger, H. Hamidov, C. R. S. Haines, P. L. Alireza, A. R. Wildes, C. Liu, S. S. Saxena, and J.-G. Park, npj Quantum Mater. **4**, 38 (2019).

[20] M. J. Coak, D. M. Jarvis, H. Hamidov, A. R. Wildes, J. A. M. Paddison, C. Liu, C. R. S. Haines, N. T. Dang, S. E. Kichanov, B. N. Savenko, S. Lee, M. Kratochvilova, S. Klotz, T. C. Hansen, D. P. Kozlenko, J. G. Park, and S. S. Saxena, Phys. Rev. X **11**, 011024 (2021).

[21] X. Ma, Y. Wang, Y. Yin, B. Yue, J. Dai, J. Cheng, J. Ji, F. Jin, F. Hong, J.-T. Wang, Q. Zhang, and X. Yu, Sci. China: Phys. Mech. Astron. **64**, 297011 (2021).

[22] Z. Chi, X. Chen, F. Yen, F. Peng, Y. Zhou, J. Zhu, Y. Zhang, X. Liu, C. Lin, S. Chu, Y. Li, J. Zhao, T. Kagayama, Y. Ma, and Z. Yang, Phys. Rev. Lett. **120**, 037002 (2018).

[23] Y. Zhou, B. Zhang, X. Chen, C. Gu, C. An, Y. Zhou, K. Cai, Y. Yuan, C. Chen, H. Wu, R. Zhang, C. Park, Y. Xiong, X. Zhang, K. Wang, and Z. Yang, Adv. Electron. Mater. **4**, 1800155 (2018).

[24] B. Yue, W. Zhong, W. Deng, T. Wen, Y. Wang, Y. Yin, P. Shan, J.-T. Wang, X. Yu, and F. Hong, J. Am. Chem. Soc. **145**, 1301 (2023).

[25] R. V. Gamernyk, Y. P. Gnatenko, P. M. Bukivskij, P. A. Skubenko, and V. Y. Slivka, J. Phys.: Condens. Matter **18**, 5323 (2006).

[26] K. Kuepper, B. Schneider, V. Caciuc, M. Neumann, A. V. Postnikov, A. Ruediger, A. A. Grabar, and Y. M. Vysochanskii, Phys. Rev. B **67**, 115101 (2003).

[27] B. Scott, M. Pressprich, R. D. Willet, and D. A. Cleary, J. Solid State Chem. **96**, 294 (1992).

[28] K. Glukhov, K. Fedyo, J. Banys, and Y. Vysochanskii, Int. J. Mol. Sci. **13**, 14356 (2012).

[29] O. Andersson, O. Chobal, I. Rizak, V. Rizak, and V. Sabadosh, Phys. Rev. B **83**, 134121 (2011).

[30] Y. Tyagur and I. Tyagur, High Press. Res. **28**, 607 (2008).

[31] V. V. Shchennikov, N. V. Morozova, I. Tyagur, Y. Tyagur, and S. V. Ovsyannikov, Appl. Phys. Lett. **99**, 212104 (2011).

[32] G. Kresse and J. Furthmüller, Phys. Rev. B **54**, 11169 (1996).

[33] P. E. Blöchl, Phys. Rev. B **50**, 17953 (1994).

[34] J. P. Perdew, A. Ruzsinszky, G. I. Csonka, O. A. Vydrov, G. E. Scuseria, L. A. Constantin, X. Zhou, and K. Burke, Phys. Rev. Lett. **100**, 136406 (2008).

[35] A. D. Becke and E. R. Johnson, J. Chem. Phys. **124**, 221101 (2006).

[36] See Supplemental Material at http://link.aps.org/supplemental/10.1103/PhysRevB.107.L140501 for the detailed experimental and computational methods; the structure of $SnPS_3$ at ambient condition (Fig. S1); the optical and electronic properties under pressure (Fig. S2); the Raman spectra under pressure (Fig. S3); the calculated bond lengths and bond angles in $SnPS_3$ under pressure (Fig. S4); the calculated phonon band structures for the high-pressure $P2_1$ phase of $SnPS_3$ at 40 GPa (Fig. S5); the lattice parameters under pressure (Fig. S6); and the coordinates of the high-pressure phase of $SnPS_3$ at 40 GPa (Table S1), which includes Refs. [26,32–35,44–49].

[37] J. A. Woollam, R. B. Somoano, and P. O'Connor, Phys. Rev. Lett. **32**, 712 (1974).

[38] A. M. Clogston, Phys. Rev. Lett. **9**, 266 (1962).

[39] L. Zhao, X. Ma, C. Tian, C. Yi, Y. Shi, F. Hong, X. Yu, Y. Han, and J.-T. Wang, Appl. Phys. Lett. **121**, 202201 (2022).

[40] S. V. Ovsyannikov, N. V. Morozova, I. V. Korobeinikov, V. Haborets, R. Yevych, Y. Vysochanskii, and V. V. Shchennikov, Dalton Trans. **46**, 4245 (2017).

[41] H. Zhu, J. Dong, P. Li, Y. Wang, Z. Guo, X. Shan, Y. Gong, P. An, X. Li, and J. Zhang, Phys. Status Solidi B **254**, 1700007 (2017).

[42] H. Aoki, J. Supercond. Novel Magn. **33**, 2341 (2020).

[43] L. Balents, C. R. Dean, D. K. Efetov, and A. F. Young, Nat. Phys. **16**, 725 (2020).

[44] K. Parlinski, Z. Q. Li, and Y. Kawazoe, Phys. Rev. Lett. **78**, 4063 (1997).

[45] H. K. Mao, J. Xu, and P. M. Bell, J. Geophys. Res.: Solid Earth **91**, 4673 (1986).

[46] M. B. Smirnov, J. Hlinka, and A. V. Solov'ev, Phys. Rev. B **61**, 15051 (2000).

[47] P. H. M. van Loosdrecht, M. M. Maior, S. B. Molnar, Y. M. Vysochanskii, P. J. M. van Bentum, and H. van Kempen, Phys. Rev. B **48**, 6014 (1993).

[48] S. V. Ovsyannikov, H. Gou, N. V. Morozova, I. Tyagur, Y. Tyagur, and V. V. Shchennikov, J. Appl. Phys. **113**, 013511 (2013).

[49] C. E. Byvik, B. T. Smith, and B. Reichman, Sol. Energy Mater. **7**, 213 (1982).